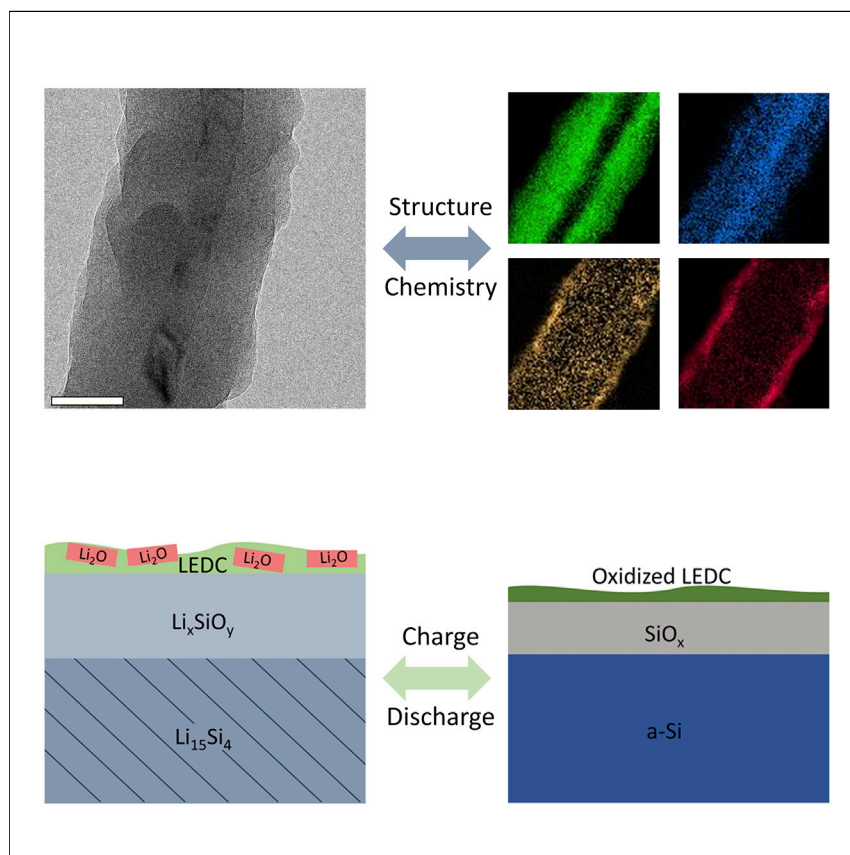


Article

Dynamic Structure and Chemistry of the Silicon Solid-Electrolyte Interphase Visualized by Cryogenic Electron Microscopy



A poor understanding of the solid-electrolyte interphase has hindered the commercialization of silicon as a next-generation lithium-ion battery anode material. Using cryogenic electron microscopy and spectroscopy, we uncover the origin of the Si anode instability in standard electrolytes, along with the role of electrolyte additives for enhanced cyclability.

William Huang, Jiangyan Wang, Michael R. Braun, ..., David T. Boyle, Paul C. McIntyre, Yi Cui
 yicui@stanford.edu

HIGHLIGHTS

Lithiated silicon is preserved and imaged in the charged state using cryo-EM

Cryo-(S)TEM and EELS reveal the nanoscale structure and chemistry of the SEI

The SEI is reversible across the first cycle in standard EC electrolytes

The additive FEC stabilizes silicon by depositing an irreversible polymer layer



Understanding

Dependency and conditional studies on material behavior

Huang et al., Matter 1, 1–14
 November 6, 2019 © 2019 Published by Elsevier Inc.
<https://doi.org/10.1016/j.matt.2019.09.020>

Article

Dynamic Structure and Chemistry of the Silicon Solid-Electrolyte Interphase Visualized by Cryogenic Electron Microscopy

William Huang,¹ Jiangyan Wang,¹ Michael R. Braun,¹ Zewen Zhang,¹ Yuzhang Li,¹ David T. Boyle,² Paul C. McIntyre,¹ and Yi Cui^{1,3,4,*}

SUMMARY

The commercialization of the silicon (Si) anode has been hindered by the instability of its solid-electrolyte interphase (SEI), yet a comprehensive understanding of SEI properties remains underdeveloped owing to the challenge of characterizing this nanoscale passivation layer. In this work, we visualize the structure and chemistry of the SEI on silicon anodes using atomic-resolution cryogenic (scanning) transmission electron microscopy (cryo-(S)TEM) and electron energy loss spectroscopy (EELS), revealing its evolution over the first cycle. We discover the origin of the Si SEI instability in ethylene carbonate (EC) electrolytes, owing to the high reversibility of the SEI. The role of the critical electrolyte additive fluoroethylene carbonate is revealed, which extends the cyclability of the Si anode through deposition of an electrochemically irreversible polycarbonate layer on the anode surface. These findings provide a nuanced view into the Si anode instability in commercial EC-based electrolytes and the role of additives for SEI stabilization.

INTRODUCTION

To sustain the increasing energy-storage demands of portable electronics and electric vehicles, high-energy-density battery chemistries are needed.¹ Next-generation lithium-ion (Li-ion) chemistries with silicon (Si) negative electrodes (anodes) are promising owing to the high specific capacity ($3,579 \text{ mAh g}^{-1}$) of Si, approximately ten times as high as that of conventional graphite anodes (371 mAh g^{-1}).²⁻⁵ However, the high lithium (Li) storage capacity of Si results in a large volume change during lithiation ($\sim 300\%$), leading to continuous fracture and reformation of the solid-electrolyte interphase (SEI),⁶ a passivation layer present on all low-potential Li-ion battery anodes. The SEI arises from the electrochemical reduction of electrolyte molecules at the low potentials of the anode and is critical to battery operation, as it kinetically stabilizes the electrolyte against the low potentials at the anode and mediates Li-ion transport between the electrolyte and electrode.^{7,8} In conventional graphitic anodes, high cycling stability is achieved due to the stability and self-limiting growth of the SEI; however, in next-generation battery anodes such as Si, the SEI is continuously fractured and reformed owing to the massive volume change of the active material, making it the principal source of capacity loss in the battery.⁹ Hence, the structure and chemistry of the SEI are critical parameters for the reversibility of the Si anode.

Given the importance of the SEI, significant effort has been expended on its characterization via X-ray photoelectron spectroscopy,¹⁰⁻¹² secondary ion mass spectrometry,^{13,14} Auger electron spectroscopy,¹⁵ and X-ray and neutron reflectometry.¹⁶⁻¹⁸

Progress and Potential

Improved lithium-ion batteries are critical to the adoption of electric vehicles. Replacing conventional graphite anodes with silicon anodes will greatly improve the energy density of next-generation lithium-ion batteries; however, progress has been hindered by a poor understanding of why silicon anodes rapidly fail. Using atomic-resolution cryogenic electron microscopy and spectroscopy, we preserve and image the silicon anode at various states of charge and identify the source of its instability in standard electrolytes. We further reveal the origin of the silicon anode stabilization in enhanced electrolytes. Our results shed light on the failure modes of silicon and guide engineered electrolytes for high-energy-density battery chemistries.

These techniques have revealed the chemistry of the SEI, with Li_xSiO_y , Li_2O , LiF , Li_2CO_3 , and organic carbonates as key components in the SEI. However, the SEI is a nanoscale structure; while these techniques give excellent spectral resolution, they probe large ensembles of the electrode surface. The arrangement of SEI species is unknown due to the challenge of structural and chemical characterization with high in-plane spatial resolution. Whereas atomic force microscopy^{19,20} and scanning electron microscopy (SEM)²¹ offer high spatial resolution but poor chemical sensitivity, transmission electron microscopy (TEM)^{22,23} has the potential to offer structural and chemical information at high spatial resolutions, but the electron beam sensitivity and air reactivity of lithiated Si precludes high-resolution analysis. Nonetheless, these studies have revealed phenomena such as the “breathing” or reversibility of the Si SEI on delithiation,^{16,18,24,25} the passivating properties of the lithiated native Si oxide,^{13,26} and the dynamics of Li insertion.^{16,27} Still, the structure and chemistry of the Si SEI have yet to be revealed at the atomic scale.

The stability of the Si anode relies critically on electrolyte additives; among the most commonly used is fluorinated ethylene carbonate (FEC). FEC is indispensable to the lifetime of the Si anode;^{28–30} however, its role on the Si SEI remains poorly understood. FEC is believed to decompose into fluoride anions, generating LiF , along with vinylene carbonate (VC) radicals, prior to reduction of other electrolyte components.^{31,32} The deposition of FEC decomposition products modifies the SEI chemistry and properties, with the performance enhancement attributed to either the deposition of electrochemically stable LiF ^{14,22,29} or elastomeric polymerized VC.^{18,21,31,33} Ultimately, the role of FEC on local SEI chemistry and its explicit role in anode stabilization is poorly understood due to the lack of high-spatial-resolution characterization techniques.

Here, we leverage recent advances in cryogenic transmission electron microscopy (cryo-TEM) to visualize the Si SEI with atomic resolution. Cryo-TEM has recently been shown to stabilize beam-sensitive and air-reactive battery materials in the TEM column at liquid nitrogen temperature and to provide high-resolution structural and chemical characterization of the SEI on the metallic Li anode^{34–36} and oxidized copper.³⁷ The SEI is commonly assumed to be a monotonically growing structure,³⁸ using this nascent technique, we stabilize the Si anode for high-resolution TEM and reveal the dynamic nanostructure and chemistry of the Si SEI upon lithiation and delithiation. Furthermore, we examine the atomistic role of the electrolyte additive FEC; using cryo-TEM, we reveal its role on the SEI structure and chemistry and link the physicochemical characteristics of the SEI to the anode cyclability. From this work, we build a more complete picture of the lithiation and delithiation of the Si SEI.

RESULTS AND DISCUSSION

Growth and Lithiation of Silicon Nanowires on the TEM Grid

TEM necessitates electron-transparent specimens; to prepare Si anodes for TEM with minimal processing, we developed a process to grow Si nanowires (NWs) directly on a TEM grid via a vapor-liquid-solid (VLS) process.^{2,39} This offers two main advantages: Si active material is electronically connected to the TEM grid current collector, eliminating the need for binder or conductive additives and thus reducing heterogeneity from porous electrode models,⁸ and eliminating the need for sample preparation such as microtomy or focused-ion beam, which may introduce chemical or mechanical artifacts.⁴⁰ Scanning electron microscopy (SEM) images of the as-grown NWs show their growth out of the TEM grid sidewalls along with their high aspect ratio (Figures 1A and 1B). High-resolution TEM (HRTEM) shows

¹Department of Materials Science and Engineering, Stanford University, Stanford, CA 94305, USA

²Department of Chemistry, Stanford University, Stanford, CA 94305, USA

³Stanford Institute for Materials and Energy Sciences, SLAC National Accelerator Laboratory, 2575 Sand Hill Road, Menlo Park, CA 94025, USA

⁴Lead Contact

*Correspondence: yicui@stanford.edu

<https://doi.org/10.1016/j.matt.2019.09.020>

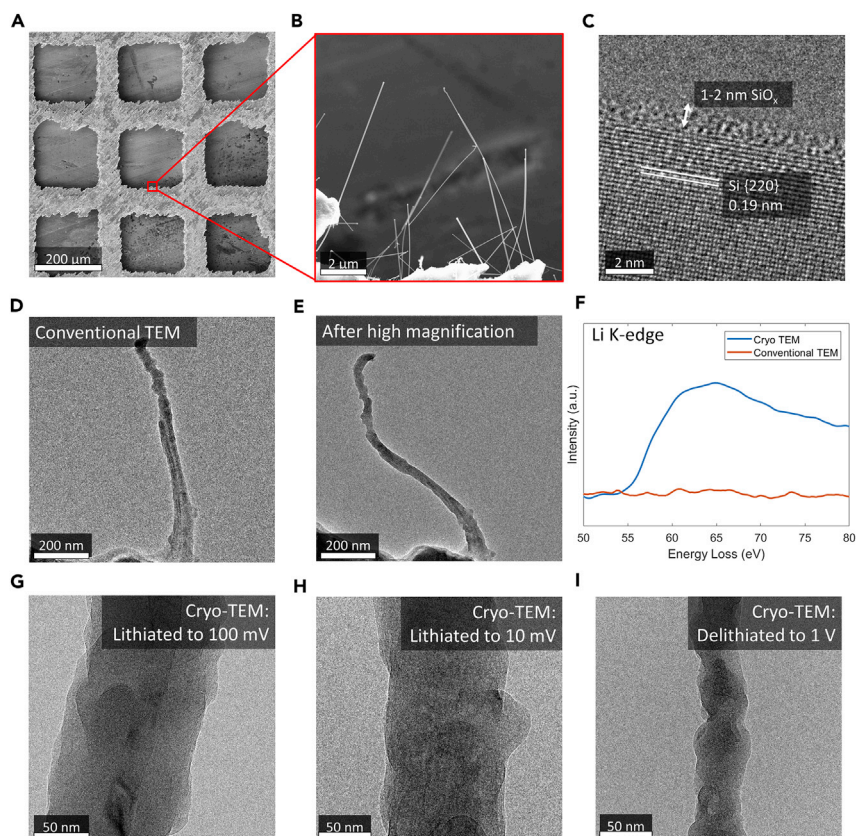


Figure 1. Growth of Si Nanowires on the TEM Grid and Comparison of Conventional and Cryo-TEM

- (A and B) SEM of the Si nanowires (NWs) grown on the TEM grid.
 (C) HRTEM of the as-grown Si NWs and native-oxide termination.
 (D) Conventional TEM of a lithiated Si NW at room temperature.
 (E) Conventional TEM of the lithiated Si NW from (D) after high-magnification imaging at room temperature.
 (F) Li K-edge EELS spectra of the lithiated Si NW after high magnification under room-temperature, conventional TEM, and cryo-TEM conditions.
 (G) Bright-field cryo-TEM of a Si NW lithiated to 100 mV.
 (H) Bright-field cryo-TEM of a Si NW lithiated to 10 mV.
 (I) Bright-field cryo-TEM of a Si NW lithiated to 10 mV, then delithiated to 1 V.

the crystallinity of the as-grown NW, along with a thin native oxide termination of 1–2 nm (Figure 1C).

We assembled Si NW TEM grid half-cells using the Si NW TEM grid as the working electrode, and lithiated the Si via linear sweep voltammetry (LSV). Owing to the large inelastic scattering cross-section of Li alloys such as Li_xSi ,⁴¹ the lithiated Si anode is highly sensitive to electron-beam-induced damage at room temperature (Figures 1D and 1E). Imaging of the lithiated Si NW TEM grid at room temperature using conventional TEM results in significant structural changes; as the image is magnified and the electron dose rate increased for HRTEM imaging, the Li_xSi undergoes structural and chemical changes (Video S1). Secondary phases nucleate out of the NW and the NW deforms under electron irradiation owing to mass loss, followed by structural stabilization once the Li atoms have been fully ejected from the NW. Electron energy loss spectroscopy (EELS) of the NW after attempted HRTEM imaging reveals an absence of the Li K-edge, indicative of selective mass loss of the weakly bonded

Li. This suggests that the secondary phase nucleated out of the NW during conventional TEM imaging is metallic Li, with amorphous, delithiated Si remaining (Figure 1F). In contrast, cryo-TEM at liquid nitrogen temperature stabilizes the Li_xSi under electron irradiation, and the Li K-edge remains robust even after HRTEM, making cryogenic stabilization requisite for accurate analysis of lithiated Si and its SEI.

Structural and Chemical Characterization of Li_xSi in Ethylene Carbonate Electrolyte

To preserve the native structure and chemistry of Li_xSi and its SEI, all following (S) TEM images presented in this work were taken under cryogenic conditions. In addition to structural and chemical stabilization under electron irradiation, cryogenic sample preparation and cryo-TEM imaging serves to prevent side reactions with air and water during sample insertion.³⁴ Si NWs were partially lithiated to 100 mV versus Li/Li⁺ in the standard Li-ion battery electrolyte of 1:1 (v/v) ethylene carbonate/diethyl carbonate (EC/DEC) with 1.0 M LiPF_6 salt, revealing an atomically abrupt interface between the crystalline Si core and an amorphous Li_xSi shell (Figures 1G and 2A), in line with previous *in situ* TEM observations.²⁷ This confirms that in real battery operating conditions with liquid electrolyte, Si lithiation proceeds radially, and crystalline Si is amorphized by Li alloying. The structure of the native-oxide-terminated NW remains amorphous beyond the crystalline Si core out to the outer SEI/vacuum interface, where the NW is terminated by a layer of crystalline Li_2O in the SEI (Figure 2B). However, owing to the lack of a resolvable interface between amorphous Li_xSi and amorphous Li_xSiO_y , the boundary between Li_xSi and the SEI is poorly defined. Through cryo-STEM EELS mapping, the SEI can be distinguished, and a core/shell/shell structure is observed consisting of a Si-rich core, a Li-rich inner shell, and a Li-, C-, and O-rich outer shell (Figure S1).

On full lithiation to 10 mV versus Li/Li⁺ (Figure 1H), amorphous Li_xSi crystallizes into $\text{Li}_{15}\text{Si}_4$, the most stable phase of Li_xSi at room temperature,⁴² and the SEI becomes distinguishable from $\text{Li}_{15}\text{Si}_4$ (Figure 2C). The lithiated native oxide, Li_xSiO_y , remains as an amorphous layer interfaced with the $\text{Li}_{15}\text{Si}_4$, possibly due to kinetic factors such as incomplete lithiation to the most lithiated phase of Li_4SiO_4 or impeded crystallization due to lattice mismatch between $\text{Li}_{15}\text{Si}_4$ and Li_4SiO_4 . Above this amorphous Li_xSiO_y is the SEI originating from the decomposition of electrolyte molecules such as EC, consisting of amorphous organic components embedded with Li_2O (Figure 2D). Comparison of the Li K-edge of the Si SEI in EC/DEC electrolyte to a Li_2O reference confirms that the SEI is rich in Li_2O (Figure S17). Structurally, the fully lithiated SEI at 10 mV is similar to the SEI of the partially lithiated NW at 100 mV, which is unsurprising considering that lithiation occurs radially; the SEI is interfaced with Li_xSi in both cases, with low potentials of 100 mV and 10 mV, far below the EC decomposition potential of 0.9 V.³⁸ Cryo-STEM EELS analysis of the carbon K-edge from the SEI reveals the strong carbonate bonding characteristic of the organic SEI components (Figure 3C), indicative of alkyl carbonate species such as Li ethylene dicarbonate (LEDC).⁴³ While the lithiation of SiO_x has been suggested to form Li_2O via a conversion reaction into Si and Li_2O ,⁴⁴ thermodynamic calculations have revealed this reaction to be improbable.⁴⁵ The positioning of the observed Li_2O on the outer interface, away from the Li_xSiO_y layer, suggests that the Li_2O arises from the decomposition of EC. This SEI nanostructure differs greatly from the “mosaic” nanostructure observed on the metallic Li anode in EC/DEC electrolyte,³⁴ likely due to the presence of the Si native oxide. This built-in passivation layer in the case of the Si anode results in an amorphous SEI at the $\text{Li}_{15}\text{Si}_4$ /SEI interface, which partially passivates the anode and increases the overpotential for EC decomposition. Further EC decomposition on top of this Li_xSiO_y layer then results in a thin, EC-derived SEI

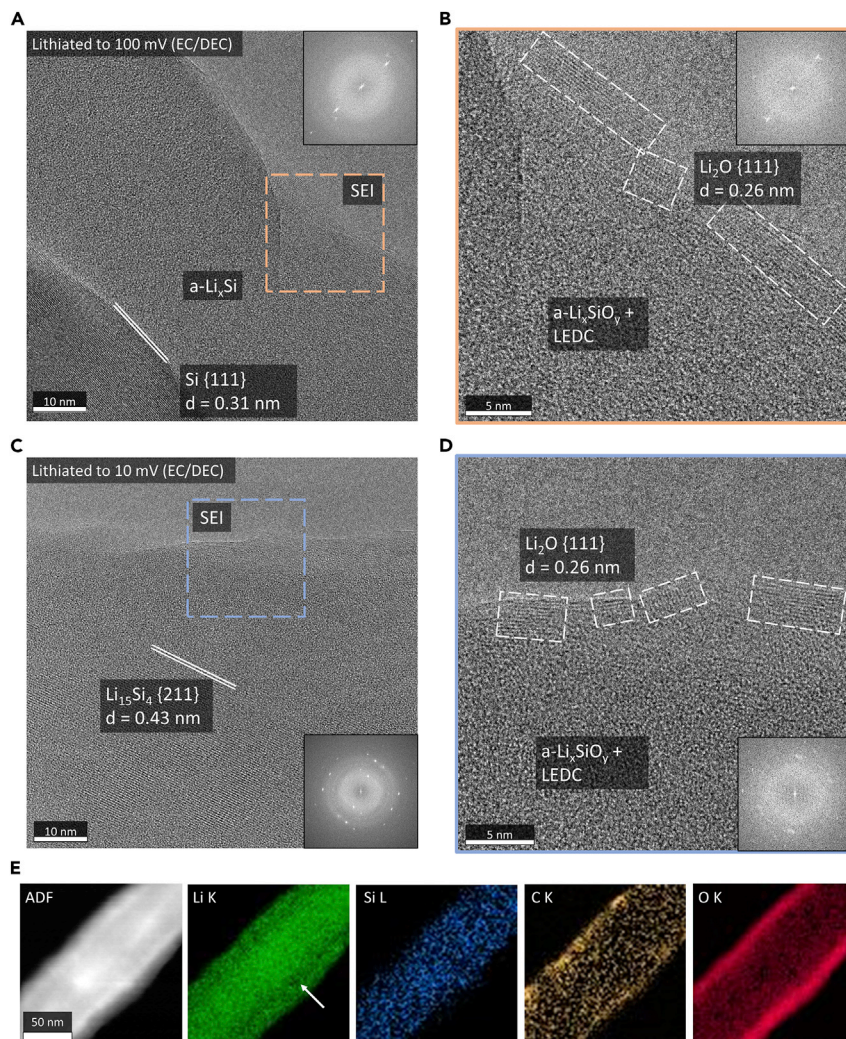


Figure 2. Lithiation of Si NWs in EC/DEC Electrolyte

(A) HRTEM of Si NW partially lithiated, to a cutoff voltage of 100 mV and (inset) fast-Fourier transform (FFT).

(B) Magnified HRTEM and FFT of the solid-electrolyte interphase (SEI).

(C) HRTEM and FFT of Si NW fully lithiated to 10 mV.

(D) Magnified HRTEM and FFT of the SEI.

(E) STEM EELS mapping of the Si NW lithiated to 10 mV. The white arrow indicates the low Li-intensity layer.

All images are acquired under cryogenic conditions.

containing LEDC, the amorphous organic product of EC decomposition, along with Li_2O from further EC reduction. The resultant SEI nanostructure is a bilayer structure, of amorphous Li_xSiO_y at the inner interface and a mixed layer of amorphous LEDC and crystalline Li_2O at the outer interface, reminiscent of the “layered” SEI nanostructure observed for Li metal grown in FEC.³⁴

Chemical distributions of anode and SEI components such as Li, Si, C, and O in the fully lithiated NW can be further revealed through Cryo-STEM EELS mapping (Figure 2E). The annular dark-field (ADF) image shows a high-intensity core consisting of $\text{Li}_{15}\text{Si}_4$, along with a lower-intensity outer shell due to a low-density SEI. ADF contrast arises from both diffraction and mass-thickness contrast;⁴⁰ the

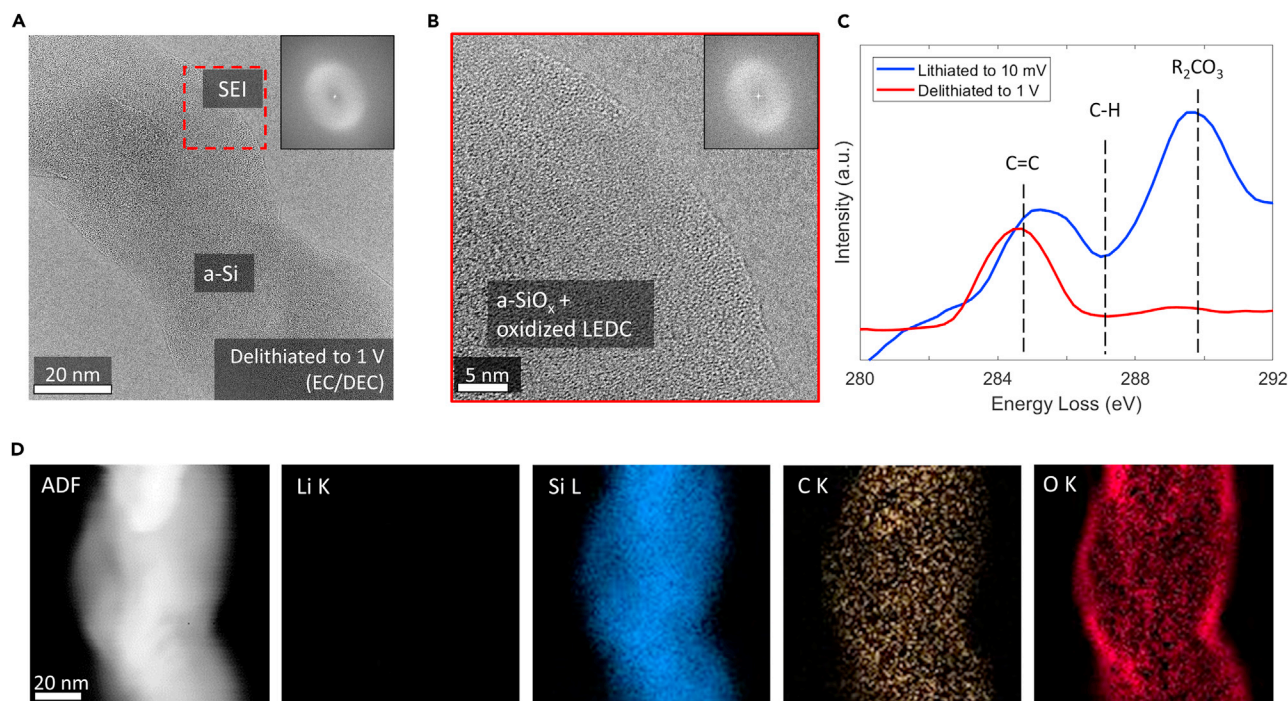


Figure 3. Delithiation of Si NWs in EC/DEC Electrolyte

(A) HRTEM and FFT of Si NW lithiated to 10 mV, then delithiated to 1 V.

(B) Magnified HRTEM and FFT of Si NW SEI.

(C) EEL spectra of the C K-edge from the Si NW edge when lithiated to 10 mV and delithiated to 1 V.

(D) STEM EELS mapping of the Si NW when delithiated to 1 V.

All images are acquired under cryogenic conditions.

high-intensity core is likely due to diffraction from crystalline $\text{Li}_{15}\text{Si}_4$ along with mass-thickness scattering from electron-dense Si. The lower intensity in the SEI arises from the weak scattering of low-density amorphous SEI components. C and O from SEI components such as LEDC, Li_2O , and Li_xSiO_y are localized to the outer shell as well, while Si remains confined to the core. Li extends throughout the entire structure, with the highest intensity in the core arising from the Li-rich $\text{Li}_{15}\text{Si}_4$ phase. The Li intensity is second highest at the outer interface, as a result of Li-rich SEI components such as LEDC and Li_2O from the EC-derived SEI. Between the Li-rich $\text{Li}_{15}\text{Si}_4$ core and the outermost Li-rich SEI is a region of lower Li intensity, indicated by the white arrow in Figure 2E, due to the relatively low Li concentrations in Li_xSiO_y . EELS is sensitive to bonding environments; the metallicly bonded Li in $\text{Li}_{15}\text{Si}_4$ exhibits a different spectral signature compared with ionically bonded Li in the SEI (Figure S2). These differing Li fine structures can be further mapped through multiple linear least squares (MLLS) fitting to delineate Li in the core from Li in the SEI (Figure S3). Despite the use of a fluorinated salt, LiPF_6 , fluorine is not detected in the EELS spectrum (Figure S4), indicating that fluorinated decomposition products such as LiF are not a principal component of the compact SEI on the Si surface, although they may exist elsewhere on the electrode surface.

Reversibility of the Si SEI on Delithiation in Ethylene Carbonate Electrolyte

We further investigated the delithiation behavior of the Si SEI in EC/DEC electrolyte (Figure 1I). On delithiation, the Si anode is amorphized, as shown in Figure 3A and its fast-Fourier transform (FFT). While the SEI is terminated by a Li_2O layer in the

lithiated state, on delithiation the SEI becomes fully amorphous (Figure 3B). This indicates reversibility of the Li_2O layer arising from EC reduction. The Li_2O delithiation reaction is further supported by selected area electron diffraction of a single NW (Figure S5); crystalline reflections from $\text{Li}_{15}\text{Si}_4$ and a polycrystalline ring from Li_2O are visible in the lithiated state; and on delithiation, broad rings characteristic of amorphous Si are evident. The polycrystalline ring from Li_2O is not detected. Evidently, the structure of the Si SEI is reversible on the first cycle.

Cryo-STEM EELS mapping of the delithiated Si NW reveals that not only the SEI nanostructure but also the chemistry is reversible. Li K-edge mapping reveals that no Li remains in the NW, confirming that the NW is fully delithiated; however, no Li is detected in the surface SEI layer (Figures 3D and S6). An oxygenated surface layer remains, and C counts become more dilute while surface enrichment of C is no longer detected. Analysis of the C K-edge fine structure with cryo-EELS reveals that the carbonate peak intensity at 290 eV is undetectable in the delithiated state, with only insulating olefinic or aromatic carbons remaining. Sparse crystalline Li_2CO_3 can be observed in some regions on the delithiated NW (Figure S7), indicating that Li_2CO_3 is a stable species against oxidation and a minority contribution to the carbonate signal in the C K-edge. Li_2CO_3 does not appear to be a majority component in the compact SEI directly on the electrode surface, likely indicating its instability against the highly reductive $\text{Li}_{15}\text{Si}_4$ surface. Indeed, simulations by Leung et al. have predicted that Li_2CO_3 is thermodynamically unstable on Li surfaces, and decomposes to Li_2O .⁴⁶ This instability was also speculated to occur on Li_xSi surfaces and is a likely pathway for the abundant Li_2O within the SEI in the lithiated state. Their calculations also predict that Li_2CO_3 is stable against Si in the delithiated state, consistent with our observations. The low intensity of any carbon-oxygen bonding in the carbon fine structure along with lack of Li counts in the SEI indicates that the surficial oxygen layer arises from SiO_x rather than Li_xSiO_y or LEDC.

These observations reveal that not only the Si lithiation but also the Si SEI are reversible. While Li_2O is thermodynamically stable against $\text{Li}_{15}\text{Si}_4$ in the lithiated state, Li_2O is reactive to Si and can form Li_xSiO_y on delithiation.^{15,46} Although Li_4SiO_4 , the most Li-rich phase of Li_xSiO_y , is reported to be irreversible,^{47–49} the lack of crystalline Li_4SiO_4 observed in the lithiated Si (Figures 2C and 2D) suggests that this phase is kinetically limited and is not reached on the first cycle. Thus, a mix of Li-poor Li_xSiO_y phases are likely formed on lithiation (and Li_2O reaction with Si on delithiation), which are delithiated on the first cycle. Furthermore, not only are the inorganic components in the SEI reversible, but so too are the organic carbonates. The reduction in carbonate peak intensity revealed with cryo-EELS reveals that EC reduction products such as LEDC are also reversible. These observations support reports of “breathing,” or reversible SEI behavior of the inorganic Si SEI components,^{16,18,25} while unifying these observations with the oxidation of organic SEI components.^{43,50} The SEI is typically thought to monotonically grow with increasing electrolyte decomposition; this is not the case, as both inorganic and organic SEI components are dynamic with state of charge. This oxidation of organic and inorganic Si SEI components may be beneficial during initial cycling of the Si anode in EC-based electrolyte; however, the lack of a stable SEI results in poor cycling stability and rapid failure of Si.

Impact of FEC on the Si SEI

While the Si anode rapidly fails in EC-based electrolyte, the electrolyte additive FEC greatly extends its cycling stability (Figure 4A) while conversely decreasing the first-cycle Coulombic efficiency (Figure 4B). The use of FEC is

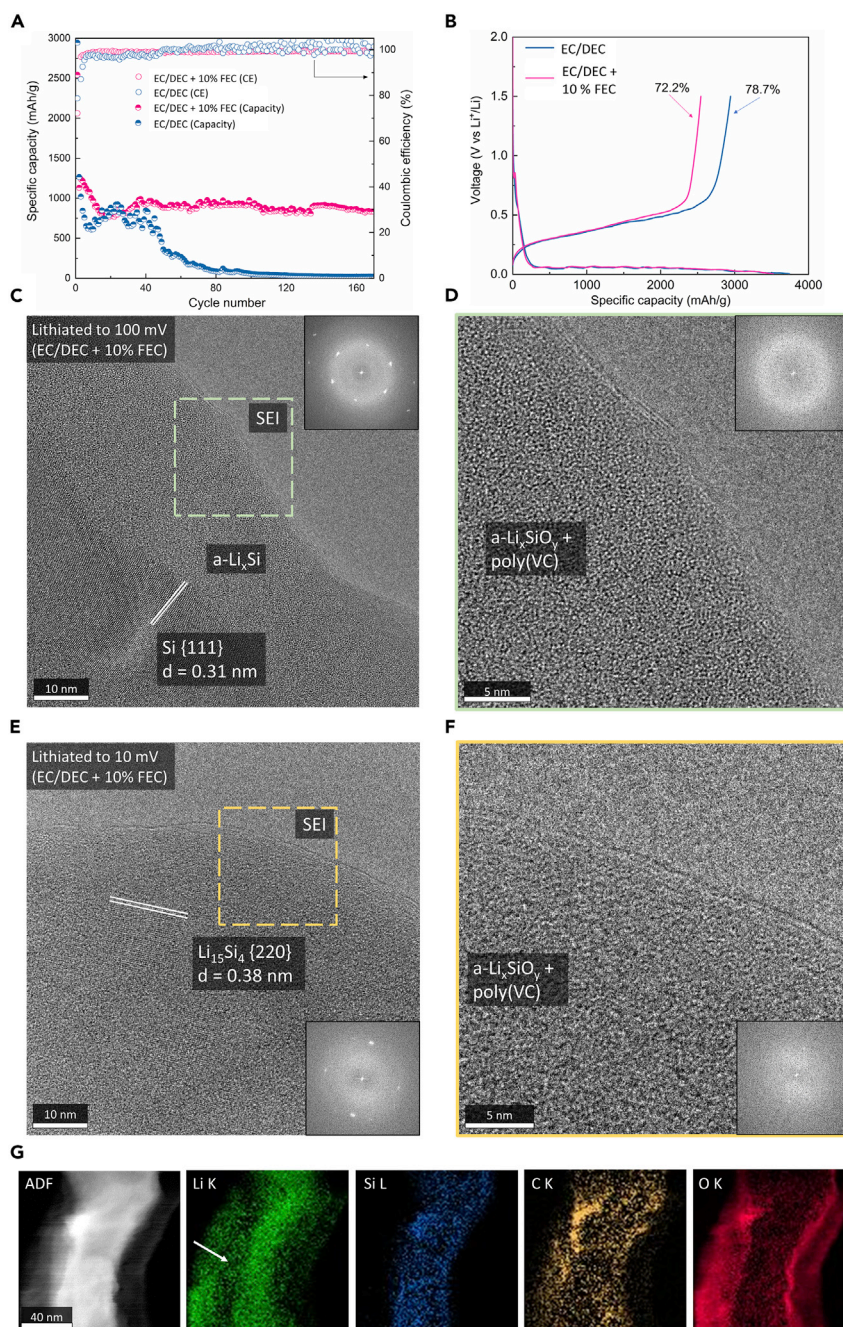


Figure 4. Lithiation of Si NWs in EC/DEC + 10% FEC Electrolyte

(A) Cycling stability of Si nanoparticle electrodes in EC/DEC and EC/DEC + 10% FEC electrolyte.
 (B) Capacity curves and initial Coulombic efficiency of the first lithiation of Si nanoparticle electrodes in EC/DEC and EC/DEC + 10% FEC.
 (C) HRTEM of Si NW partially lithiated, to a cutoff voltage of 100 mV and (inset) FFT.
 (D) Magnified HRTEM and FFT of the SEI.
 (E) HRTEM and FFT of Si NW fully lithiated to 10 mV.
 (F) Magnified HRTEM and FFT of the SEI.
 (G) STEM EELS mapping of the Si NW lithiated to 10 mV. The white arrow indicates the low Li-intensity layer.
 All images are acquired under cryogenic conditions.

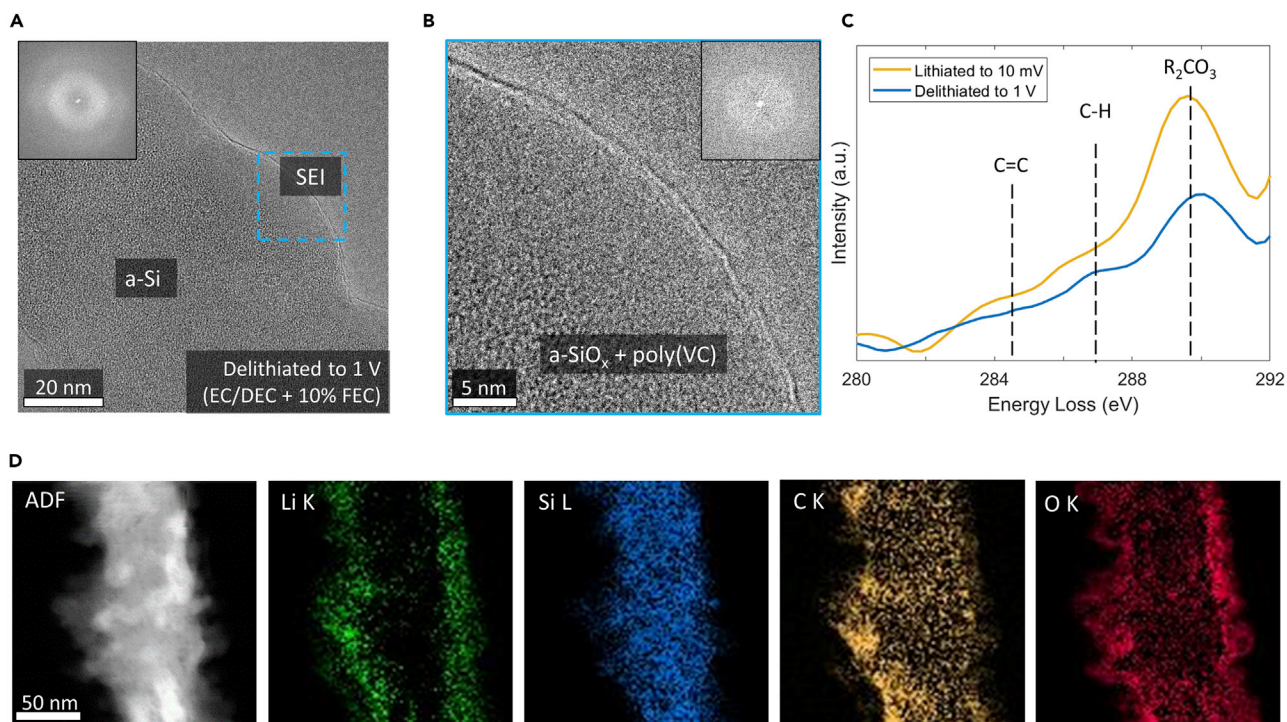


Figure 5. Delithiation of Si NWs in EC/DEC + 10% FEC Electrolyte

(A) HRTEM and FFT of Si NW lithiated to 10 mV, then delithiated to 1 V.

(B) Magnified HRTEM and FFT of Si NW SEI.

(C) EEL spectra of the C K-edge from the Si NW edge when lithiated to 10 mV and delithiated to 1 V.

(D) STEM EELS mapping of the Si NW when delithiated to 1 V.

All images are acquired under cryogenic conditions.

clearly advantageous to the Si anode lifetime; in this section, we discuss its impact on the SEI chemistry and structure. The lithiation behavior of Si in EC/DEC + 10 vol % FEC proceeds similarly to Si in EC/DEC electrolyte alone; at 100 mV, a crystalline Si core is surrounded by an amorphous Li_xSi shell (Figure 4C). When fully lithiated to 10 mV, the Li_xSi crystallizes to Li₁₅Si₄ (Figure 4E), verifying that FEC does not change lithiation dynamics, and that the SEI is the main source of increased performance. Closer inspection of the Si SEI in EC/DEC + 10% FEC reveals a drastic change in SEI nanostructure; the Si SEI is fully amorphous (Figures 4D and 4F), consisting of the lithiated SiO_x, Li_xSiO_y, along with an amorphous outer layer. The lack of fluorine (Figure S8) and strong carbonate signal in the C K-edge (Figure 5C) confirms this amorphous outer layer is not amorphous LiF, but rather polycarbonates arising from VC polymerization. The Li₂O layer seen in the case of Si lithiated in EC/DEC is absent, further reinforcing that Li₂O arises from EC decomposition rather than from conversion of SiO_x. The SEI formed in the presence of FEC thus consists of an amorphous bilayer structure, with amorphous Li_xSiO_y on the inner interface and an amorphous poly(VC) layer on the outer interface. While Li_xSiO_y partially passivates the Li₁₅Si₄ surface, the poly(VC) layer completes the passivation, inhibiting further decomposition of EC into LDC and Li₂O. Cryo-STEM EELS mapping reveals the SEI is rich in Li, C, and O, elementally similar to the SEI formed in EC-based electrolyte. The Li spectra can be further mapped to the different bonding environments in the core and SEI through MLLS fitting, as discussed previously (Figures S9 and S10). Only with high-resolution imaging through Cryo-HRTEM can the SEI structure be unambiguously resolved.

On lithiation it can be observed that the SEI nanostructure is altered by the addition of FEC, and is fully amorphous due to poly(VC) deposition. Still, the source of the enhanced cycling stability of the Si anode with the FEC additive is not immediately obvious. Inspection of the Si in the delithiated state reveals the conversion to amorphous Si, maintaining an amorphous interphase (Figures 5A and 5B). The C K-edge of the SEI reveals a persistent carbonate peak in the delithiated state, indicative of an electrochemically stable poly(VC) layer coating the NW surface (Figure 5C), along with a strong Li K-edge peak (Figure S11). Whereas Cryo-EELS revealed the oxidation of organic carbonates such as LEDC in the EC-derived SEI, with the addition of FEC, an organic polycarbonate SEI is formed that is stable against oxidation. Cryo-STEM EELS mapping of the delithiated Si NW with FEC additive, shown in Figure 5D, reveals a low-density surface layer in the ADF image, coincident with a Li-, C-, and O-rich surface layer. While the O map likely has contributions from SiO_x as well as poly(VC), the Li and C map indicates the presence of lithiated organic species such as poly(VC), even in the delithiated state. In comparison, the delithiated $\text{Li}_{15}\text{Si}_4$ in EC alone showed no Li and reduced C in the SEI.

The beneficial role of FEC is thus to polymerize on the NW surface, forming a conformal poly(VC) SEI that is stable against oxidation. The irreversibility of the FEC-derived SEI is thus reflected in the first-cycle Coulombic efficiency; while Si cycled in EC alone exhibits a higher initial Coulombic efficiency (ICE) owing to the oxidation of SEI components, the Si cycled in FEC is stable on delithiation, leading to a lower ICE. The low ICE of Si cycled with FEC is accordingly coupled to its late-cycle stability. In addition to its electrochemical stability, this poly(VC) coating readily crosslinks, giving the SEI elastomeric behavior.³¹ These elastomeric properties likely contribute to the stability as well, maintaining a conformal SEI as the Si repeatedly cycles and undergoes massive volume changes. We thus reveal the role of FEC on the cycling stability of Si; FEC decomposition results in the polymerization of VC radicals on the anode surface, resulting in an amorphous SEI with a bilayer structure: an inner layer of Li_xSiO_y characteristic of native-oxide-terminated Si, with an outer layer of poly(VC). The poly(VC) layer grants electrochemical and mechanical stability to the SEI owing to its resistance to oxidation and elastomeric properties. LiF is not detected in appreciable quantities within the SEI, and we instead ascribe the performance enhancement of FEC to the polymerization of VC radicals.

Conclusion

Through a combination of cryo-(S)TEM and EELS, we stabilize Li_xSi for electron microscopy and spectroscopy and reveal the structure and chemistry of the SEI on the Si anode across the first cycle. In standard EC/DEC electrolyte, the lithiated Si ($\text{Li}_{15}\text{Si}_4$) is interfaced with a bilayer SEI, consisting of an inner amorphous layer from the lithiation of the SiO_x , yielding amorphous Li_xSiO_y , and an outer layer arising from EC decomposition, consisting of amorphous LEDC and crystalline Li_2O . On delithiation, the SEI exhibits structural and chemical reversibility; Li_2O reacts with Si to form Li_xSiO_y , which can be further delithiated, and organic carbonates such as LEDC are oxidized. With the addition of the electrolyte additive FEC, an amorphous SEI is formed on lithiation, consisting of organic poly(VC) deposition over an inner, inorganic layer of Li_xSiO_y . We attribute the enhanced stability of the Si anode in FEC to the delithiation behavior of the FEC-derived SEI; on delithiation, the poly(VC) components are stable against oxidation and a conformal SEI remains on the anode surface. These observations are graphically depicted in Figure 6. The studies herein unambiguously image the dynamic structure and chemistry of the Si SEI, and further the understanding of the role of electrolyte additives toward the stability of the Si anode.

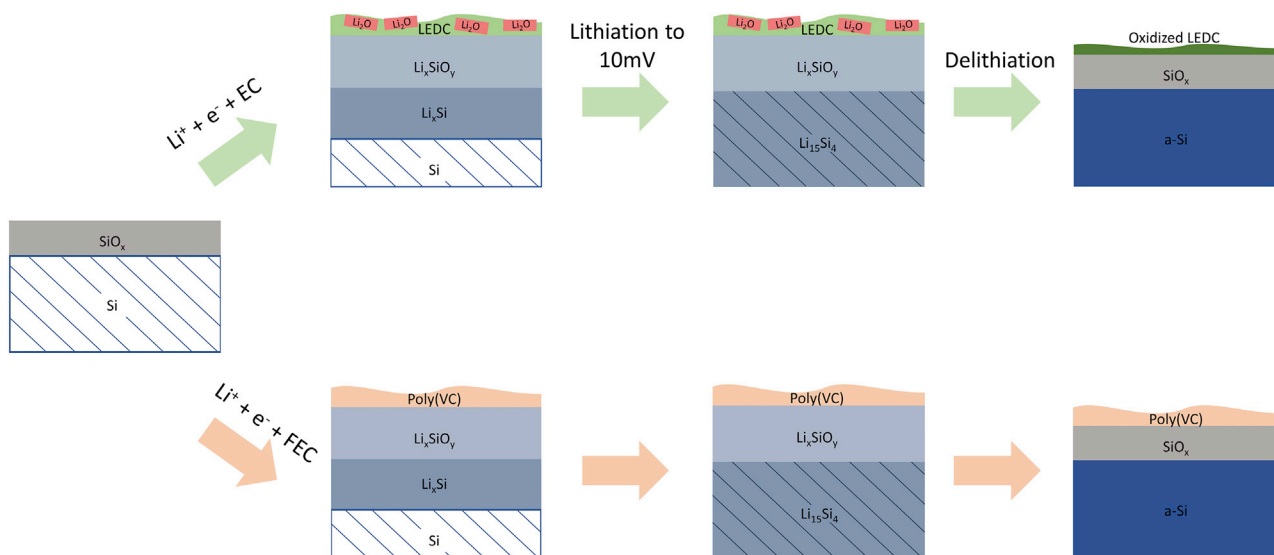


Figure 6. Schematic of the Lithiation of Oxide-Terminated Si in EC/DEC and EC/DEC + 10% FEC Electrolyte

EXPERIMENTAL PROCEDURES

Silicon NW Synthesis

Si NWs were grown via a one-step gold-catalyzed VLS growth method in a load-locked, lamp-heated, rapid-thermal, 8-inch quartz cold-wall chemical vapor deposition chamber with a base pressure of $\sim 3 \times 10^{-7}$ Torr. Si NWs were grown on stainless-steel TEM grids (100 mesh, SPI supplies) soaked in an HF acidified 40-nm gold colloidal solution (Alfa Aesar J67001 and Sigma 741981). Silane (SiH_4) was used as the Si source at a partial pressure of 0.7 Torr, diluted with hydrogen to a total pressure of 30 Torr. The colloid-coated TEM grids were annealed at 530°C in pure hydrogen for 4 min before a 30-min growth step at 530°C . NWs have an approximate diameter of 50 nm (Figures S12 and S13).

Lithiation and Delithiation of Silicon NW TEM Grids

Type 2032 coin cells were assembled in an argon glovebox with a polymer separator (Celgard 2325), Li metal foil (Alfa Aesar) as the counter/reference electrode, and a Si NW TEM grid as the working electrode. The electrolyte used was 1.0 M LiPF_6 in 1:1 (w/w) EC/DEC. In studies with FEC electrolyte additive, 1.0 M LiPF_6 in 90 vol % 1:1 (v/v) EC/DEC and 10 vol % fluoroethylene carbonate was used. In all cases, cells were assembled with 75 μL of electrolyte.

Lithiation and delithiation were achieved using LSV at 0.05 mV s^{-1} (Biologic VMP3) owing to the low capacity of the Si NW TEM grid. After reaching the voltage of interest, the cell was maintained at that voltage for 8 h before disassembly (Figure S14). For delithiation, the potential was swept to 10 mV, held at 8 h at 10 mV, followed by a linear voltage scan to 1 V and a potentiostatic hold at 1 V for 8 h (Figure S15). Separate specimens were prepared at each individual voltage due to the difficulty in recovering the same specimen from the TEM column.

Electrochemical Performance Measurements

Working electrodes were all prepared using a conventional slurry method. Si nanoparticles, carbon black conductive additive (TIMCAL Super P), and polyvinylidene fluoride (Kynar HSV 900) binder with a mass ratio of 8:1:1 were dispersed in *N*-methyl-2-pyrrolidone (NMP) and stirred for 12 h. After casting onto a 10- μm -thick

Cu foil and drying at 60°C in a vacuum oven for 12 h, the samples were calendared and cut into 1-cm² circular disks with a mass loading of ~1.0 mg cm⁻². In an argon-filled glovebox, these working electrodes were assembled into type 2032 coin cells with a polymer separator (Celgard 2325) and Li metal (Alfa Aesar) as the counter/reference electrode. One hundred microliters of 1.0 M LiPF₆ in 1:1 (w/w) EC/DEC, or 1.0 M LiPF₆ in 90 vol % 1:1 (w/w) EC/DEC with 10 vol % fluoroethylene carbonate was added as the electrolyte with full wetting of both working and counter electrode surfaces. Coin cells were loaded into a battery tester (Land Instruments) and cycled between 0.01 and 1 V at a C-rate of C/4 (To fully activate the Si electrode, the first cycle is cycled between 0.005 and 1.5 V at a C-rate of C/20). Charge/discharge rates were calculated assuming the theoretical capacity of Si (4,200 mAh g⁻¹). Coulombic efficiency was calculated using the ratio of delithiation (C_{dealloy}) capacity to lithiation (C_{alloy}) capacity ($C_{\text{dealloy}}/C_{\text{alloy}} \times 100\%$).

Cryogenic Sample Preparation

The batteries were disassembled in an argon-filled glovebox and rinsed with DEC to remove Li salts. Our rinsing procedure attempts to minimize artifacts by using minimal force and solvent volume; approximately 50 μL was carefully dropped onto the TEM grid after the battery was disassembled. Immediately after rinsing, the sample was sealed in an airtight container, submerged in liquid nitrogen, and the container crushed to rapidly expose the sample to cryogen without any air exposure. While immersed in liquid nitrogen, the sample was loaded into the cryo-EM holder (Gatan 626) and inserted into the TEM column. The cryo-EM holder uses a specialized shutter to prevent air exposure and condensation onto the sample, which preserves the specimen in its native state. Once inside the TEM column, the temperature was maintained at approximately -178°C.

Electron Microscopy

All conventional and cryo-(S)TEM characterizations were carried out using an FEI Titan 80-300 environmental (scanning) transmission electron microscope operated at an accelerating voltage of 300 kV with an energy resolution of 1 eV. The instrument is equipped with an aberration corrector in the image-forming lens, which was tuned before each sample analysis. The dose rate for HRTEM imaging was 1000 e⁻ Å² s⁻¹ with an exposure of 0.15–0.3 s using a Gatan OneView CMOS camera. The beam was blanked between images to minimize total e⁻ dose. Cryo-STEM EELS characterization was performed with a C2 aperture of 50 μm, a beam current of 8 pA, a camera length of 48 mm, and a pixel dwell time of 50 ms. These settings give a convergence angle of 9.3 mrad and an acceptor angle of 27.8 mrad. EELS spectra were acquired on a GIF Quantum 966 with a dispersion of 0.25 eV/channel in Dual EELS mode, with the low-loss centered on the zero-loss peak and the core-loss centered on the C K-edge. Thus, the Li K-, Si L-, C K-, O K-, and F K-edges can be simultaneously acquired. Energy drift during spectrum imaging was corrected by centering the zero-loss peak to 0 eV at each pixel. Maps were computed through a two-window method, with a pre-edge window fitted to a power-law background and a post-edge window of 20–40 eV on the core-loss signal. EELS spectra were summed over many pixels along the Si NW edge and smoothed with a Savitsky-Golay filter. The unfiltered spectra are presented in [Supplemental Information \(Figure S16\)](#). SEM characterization was carried out using an FEI Magellan 400 XHR scanning electron microscope. Larger versions of all HRTEM images are available in [Supplemental Information](#).

SUPPLEMENTAL INFORMATION

Supplemental Information can be found online at <https://doi.org/10.1016/j.matt.2019.09.020>.

ACKNOWLEDGMENTS

We acknowledge R.A. Vila for assistance with EELS reference spectra acquisition. Y.C. acknowledges support from the Assistant Secretary for Energy Efficiency and Renewable Energy, Office of Vehicle Technologies of the US Department of Energy under the Battery Materials Research Program. M.R.B. acknowledges NSF Graduate Fellowship (DGE – 1656518). Part of this work was performed at the Stanford Nano Shared Facilities, supported by the National Science Foundation under award ECCS-1542152.

AUTHOR CONTRIBUTIONS

W.H. and Y.C. conceived the project and designed the experiments. W.H., Y.L., and Z.Z. carried out SEM and TEM. J.W. and D.T.B. performed electrochemical characterizations. M.R.B. and P.C.M. performed materials synthesis. W.H. and Y.C. co-wrote the manuscript, with input from all authors.

DECLARATION OF INTERESTS

The authors declare no competing interests.

Received: July 12, 2019

Revised: August 20, 2019

Accepted: September 26, 2019

Published: October 30, 2019

REFERENCES

1. Chu, S., Cui, Y., and Liu, N. (2016). The path towards sustainable energy. *Nat. Mater.* *16*, 16–22.
2. Chan, C.K., Peng, H., Liu, G., McIlwrath, K., Zhang, X.F., Huggins, R.A., and Cui, Y. (2008). High-performance lithium battery anodes using silicon nanowires. *Nat. Nanotechnol.* *3*, 31–35.
3. Wu, H., and Cui, Y. (2012). Designing nanostructured Si anodes for high energy lithium ion batteries. *Nano Today* *7*, 414–429.
4. Liu, Y., Zhou, G., Liu, K., and Cui, Y. (2017). Design of complex nanomaterials for energy storage: past success and future opportunity. *Acc. Chem. Res.* *50*, 2895–2905.
5. Sun, Y., Liu, N., and Cui, Y. (2016). Promises and challenges of nanomaterials for lithium-based rechargeable batteries. *Nat. Energy* *1*, <https://doi.org/10.1038/nenergy.2016.71>.
6. Wu, H., Chan, G., Choi, J.W., Ryu, I., Yao, Y., McDowell, M.T., Lee, S.W., Jackson, A., Yang, Y., Hu, L., and Cui, Y. (2012). Stable cycling of double-walled silicon nanotube battery anodes through solid-electrolyte interphase control. *Nat. Nanotechnol.* *7*, 310–315.
7. Peled, E., and Menkin, S. (2017). Review—SEI: past, present and future. *J. Electrochem. Soc.* *164*, A1703–A1719.
8. Pinson, M.B., and Bazant, M.Z. (2012). Theory of SEI formation in rechargeable batteries: capacity fade, accelerated aging and lifetime prediction. *J. Electrochem. Soc.* *160*, A243–A250.
9. Dupré, N., Moreau, P., De Vito, E., Quazuguel, L., Boniface, M., Bordes, A., Rudisch, C., Bayle-Guillemaud, P., and Guyomard, D. (2016). Multiprobe study of the solid electrolyte interphase on silicon-based electrodes in full-cell configuration. *Chem. Mater.* *28*, 2557–2572.
10. Chan, C.K., Ruffo, R., Hong, S.S., and Cui, Y. (2009). Surface chemistry and morphology of the solid electrolyte interphase on silicon nanowire lithium-ion battery anodes. *J. Power Sources* *189*, 1132–1140.
11. Philippe, B., Dedyvère, R., Gorgoi, M., Rensmo, H., Gonbeau, D., and Edström, K. (2013). Role of the LiPF₆ salt for the long-term stability of silicon electrodes in Li-ion batteries—a photoelectron spectroscopy study. *Chem. Mater.* *25*, 394–404.
12. Philippe, B., Dedyvère, R., Allouche, J., Lindgren, F., Gorgoi, M., Rensmo, H., Gonbeau, D., and Edström, K. (2012). Nanosilicon electrodes for lithium-ion batteries: interfacial mechanisms studied by hard and soft X-ray photoelectron spectroscopy. *Chem. Mater.* *24*, 1107–1115.
13. Schroder, K.W., Dylla, A.G., Harris, S.J., Webb, L.J., and Stevenson, K.J. (2014). Role of surface oxides in the formation of solid-electrolyte interphases at silicon electrodes for lithium-ion batteries. *ACS Appl. Mater. Interfaces* *6*, 21510–21524.
14. Schroder, K., Alvarado, J., Yersak, T.A., Li, J., Dudney, N., Webb, L.J., Meng, Y.S., and Stevenson, K.J. (2015). The effect of fluoroethylene carbonate as an additive on the solid electrolyte interphase on silicon lithium-ion electrodes. *Chem. Mater.* *27*, 5531–5542.
15. Radvanyi, E., De Vito, E., Porcher, W., and Jouanneau Si Larbi, S. (2014). An XPS/AES comparative study of the surface behaviour of nano-silicon anodes for Li-ion batteries. *J. Anal. At. Spectrom.* *29*, 1120–1131.
16. Cao, C., Steinrück, H.G., Shyam, B., and Toney, M.F. (2017). The atomic scale electrochemical lithiation and delithiation process of silicon. *Adv. Mater. Interfaces* *4*, 1700771.
17. Cao, C., Iwnetu Abate, I., Sivonxay, E., Shyam, B., Jia, C., Moritz, B., Devereaux, T.P., Persson, K.A., Steinruck, H.-G., and Toney, M.F. (2019). Solid electrolyte interphase on native oxide-terminated silicon anodes for Li-ion batteries. *Joule*. <https://doi.org/10.1016/J.JOULE.2018.12.013>.
18. Veith, G.M., Doucet, M., Sacci, R.L., Vacaliuc, B., Baldwin, J.K., and Browning, J.F. (2017). Determination of the solid electrolyte interphase structure grown on a silicon electrode using a fluoroethylene carbonate additive. *Sci. Rep.* *7*, 6326.
19. Martin, L., Martinez, H., Ulldemolins, M., Pecquenard, B., and Le Cras, F. (2012). Evolution of the Si electrode/electrolyte interface in lithium batteries characterized by XPS and AFM techniques: the influence of vinylene carbonate additive. *Solid State Ionics* *215*, 36–44.
20. Breitung, B., Baumann, P., Sommer, H., Janek, J., and Brezesinski, T. (2016). In situ and operando atomic force microscopy of high-capacity nano-silicon based electrodes for lithium-ion batteries. *Nanoscale* *8*, 14048–14056.

21. Etacheri, V., Haik, O., Goffer, Y., Roberts, G.A., Stefan, I.C., Fasching, R., and Aurbach, D. (2012). Effect of fluoroethylene carbonate (FEC) on the performance and surface chemistry of Si-nanowire li-ion battery anodes. *Langmuir* **28**, 965–976.
22. Nie, M., Abraham, D.P., Chen, Y., Bose, A., and Lucht, B.L. (2013). Silicon solid electrolyte interphase (SEI) of lithium ion battery characterized by microscopy and spectroscopy. *J. Phys. Chem. C* **117**, 13403–13412.
23. Sina, M., Alvarado, J., Shobukawa, H., Alexander, C., Manichev, V., Feldman, L., Gustafsson, T., Stevenson, K.J., and Meng, Y.S. (2016). Direct visualization of the solid electrolyte interphase and its effects on silicon electrochemical performance. *Adv. Mater. Interfaces* **3**, 1600438.
24. Fears, T.M., Doucet, M., Browning, J.F., Baldwin, J.K., Winiarz, J.G., Kaiser, H., Taub, H., Sacci, R.L., and Veith, G.M. (2016). Evaluating the solid electrolyte interphase formed on silicon electrodes: a comparison of ex situ X-ray photoelectron spectroscopy and in situ neutron reflectometry. *Phys. Chem. Chem. Phys.* **18**, 13927–13940.
25. Veith, G.M., Doucet, M., Sacci, R.L., Vacaliuc, B., Baldwin, J.K., and Browning, J.F. (2015). Direct determination of solid-electrolyte interphase thickness and composition as a function of state of charge on a silicon anode. *J. Phys. Chem. C* **119**, 20339–20349.
26. McDowell, M.T., Lee, S.W., Ryu, I., Wu, H., Nix, W.D., Choi, J.W., and Cui, Y. (2011). Novel size and surface oxide effects in silicon nanowires as lithium battery anodes. *Nano Lett.* **11**, 4018–4025.
27. Liu, X.H., Wang, J.W., Huang, S., Fan, F., Huang, X., Liu, Y., Krylyuk, S., Yoo, J., Dayeh, S.A., Davydov, A.V., et al. (2012). In situ atomic-scale imaging of electrochemical lithiation in silicon. *Nat. Nanotechnol.* **7**, 749–756.
28. Lin, Y.M., Klavetter, K.C., Abel, P.R., Davy, N.C., Snider, J.L., Heller, A., and Mullins, C.B. (2012). High performance silicon nanoparticle anode in fluoroethylene carbonate-based electrolyte for Li-ion batteries. *Chem. Commun. (Camb.)* **48**, 7268–7270.
29. Choi, N.S., Yew, K.H., Lee, K.Y., Sung, M., and Kim, S.-S. (2006). Effect of fluoroethylene carbonate additive on interfacial properties of silicon thin-film electrode. *J. Power Sources* **161**, 1254–1259.
30. Xu, C., Lindgren, F., Philippe, B., Gorgoi, M., Björefors, F., and Edström, K. (2015). Improved performance of the silicon anode for li-ion batteries: understanding the surface modification mechanism of fluoroethylene carbonate as an effective electrolyte additive. *Chem. Mater.* **27**, 2591–2599.
31. Shkrob, I.A., Wishart, J.F., and Abraham, D.P. (2015). What makes fluoroethylene carbonate different? *J. Phys. Chem. C* **119**, 14954–14964.
32. Jaumann, T., Balach, J., Langklotz, U., Sauchuk, V., Fritsch, M., Michaelis, A., Teltevsikij, V., Mikhailova, D., Oswald, S., Klose, M., et al. (2017). Lifetime vs. rate capability: understanding the role of FEC and VC in high-energy Li-ion batteries with nano-silicon anodes. *Energy Storage Mater.* **6**, 26–35.
33. Jaumann, T., Balach, J., Klose, M., Oswald, S., Langklotz, U., Michaelis, A., Eckert, J., and Giebeler, L. (2015). SEI-component formation on sub 5 nm sized silicon nanoparticles in Li-ion batteries: the role of electrode preparation, FEC addition and binders. *Phys. Chem. Chem. Phys.* **17**, 24956–24967.
34. Li, Y., Pei, A., Yan, K., Sun, Y., Wu, C.L., Joubert, L.M., Chin, R., Koh, A.L., Yu, Y., Perrino, J., et al. (2017). Atomic structure of sensitive battery materials and interfaces revealed by cryo-electron microscopy. *Science* **358**, 506–510.
35. Wang, X., Zhang, M., Alvarado, J., Wang, S., Sina, M., Lu, B., Bouwer, J., Xu, W., Xiao, J., Zhang, J.G., et al. (2017). New insights on the structure of electrochemically deposited lithium metal and its solid electrolyte interphases via cryogenic TEM. *Nano Lett.* **17**, 7606–7612.
36. Zachman, M.J., Tu, Z., Choudhury, S., Archer, L.A., and Kourkoutis, L.F. (2018). Cryo-STEM mapping of solid-liquid interfaces and dendrites in lithium-metal batteries. *Nature* **560**, 345–349.
37. Huang, W., Boyle, D.T., Li, Y., Li, Y., Pei, A., Chen, H., and Cui, Y. (2019). Nanostructural and electrochemical evolution of the solid-electrolyte interphase on CuO nanowires revealed by cryogenic-electron microscopy and impedance spectroscopy. *ACS Nano* **13**, 737–744.
38. Attia, P.M., Das, S., Harris, S.J., Bazant, M.Z., and Chueh, W.C. (2019). Electrochemical kinetics of SEI growth on carbon black: part I. Experiments. *J. Electrochem. Soc.* **166**, 97–106.
39. Wagner, R.S., and Ellis, W.C. (1964). Vapor-liquid-solid mechanism of single crystal growth. *Appl. Phys. Lett.* **4**, 89–90.
40. Williams, D.B., and Carter, C.B. (2009). *Transmission Electron Microscopy: A Textbook for Materials Science (Springer)*. <https://doi.org/10.1007/978-0-387-76501-3>.
41. Wang, F., Graetz, J., Moreno, M.S., Ma, C., Wu, L., Volkov, V., and Zhu, Y. (2011). Chemical distribution and bonding of lithium in intercalated graphite: identification with optimized electron energy loss spectroscopy. *ACS Nano* **5**, 1190–1197.
42. Gu, M., Wang, Z., Connell, J.G., Perea, D.E., Lahun, L.J., Gao, F., and Wang, C. (2013). Electronic origin for the phase transition from amorphous Li₁₀Si to crystalline Li₁₅Si₄. *ACS Nano* **7**, 6303–6309.
43. Liu, T., Lin, L., Bi, X., Tian, L., Yang, K., Liu, J., Li, M., Chen, Z., Lu, J., Amine, K., et al. (2019). In situ quantification of interphasial chemistry in Li-ion battery. *Nat. Nanotechnol.* **14**, 50–56.
44. He, Y., Piper, D.M., Gu, M., Travis, J.J., George, S.M., Lee, S.H., Genc, A., Pullan, L., Liu, J., Mao, S.X., et al. (2014). In situ transmission electron microscopy probing of native oxide and artificial layers on silicon nanoparticles for lithium ion batteries. *ACS Nano* **8**, 11816–11823.
45. Saint, J., Morcrette, M., Larcher, D., Laffont, L., Beattie, S., Pérès, J.-P., Talaga, D., Couzi, M., and Tarascon, J.-M. (2007). Towards a fundamental understanding of the improved electrochemical performance of silicon-carbon composites. *Adv. Funct. Mater.* **17**, 1765–1774.
46. Leung, K., Soto, F., Hankins, K., Balbuena, P.B., and Harrison, K.L. (2016). Stability of solid electrolyte interphase components on lithium metal and reactive anode material surfaces. *J. Phys. Chem. C* **120**, 6302–6313.
47. Yu, B.C., Hwa, Y., Park, C.M., and Sohn, H.J. (2013). Reaction mechanism and enhancement of cyclability of SiO anodes by surface etching with NaOH for Li-ion batteries. *J. Mater. Chem. A* **1**, 4820–4825.
48. Wang, J., Zhao, H., He, J., Wang, C., and Wang, J. (2011). Nano-sized SiO_x/C composite anode for lithium ion batteries. *J. Power Sources* **196**, 4811–4815.
49. Kim, T., Park, S., and Oh, S.M. (2007). Solid-state NMR and electrochemical dilatometry study on Li⁺ uptake/extraction mechanism in SiO electrode. *J. Electrochem. Soc.* **154**, A1112.
50. Zhuo, Z., Lu, P., Delacourt, C., Qiao, R., Xu, K., Pan, F., Harris, S.J., and Yang, W. (2018). Breathing and oscillating growth of solid-electrolyte-interphase upon electrochemical cycling. *Chem. Commun.* **54**, 814–817.